

The transition to the ultimate regime of thermal convection from a stochastic one-dimensional turbulence perspective

Marten Klein¹† and Heiko Schmidt¹

¹Department of Numerical Fluid and Gas Dynamics, Brandenburg University of Technology (BTU) Cottbus-Senftenberg, Siemens-Halske-Ring 14, D-03046 Cottbus, Germany

(Received xx; revised xx; accepted xx)

The Rayleigh number Ra dependence of the Nusselt number Nu in turbulent Rayleigh–Bénard convection is numerically investigated for a moderate and low Prandtl number, $Pr = 0.7$ and 0.021 , respectively. Here we specifically address the case of a Boussinesq fluid in a planar configuration with smooth horizontal walls and notionally infinite aspect ratio. Numerical simulations up to $Ra = 10^{16}$ for $Pr = 0.7$ and up to $Ra = 8 \times 10^{13}$ for $Pr = 0.021$ are made feasible on state-of-the-art workstations by utilising the stochastic one-dimensional turbulence (ODT) model. The ODT model parameters were estimated once for two combinations (Pr, Ra) in the classical regime and kept fixed afterwards in order to address the predictive capabilities of the model. The ODT results presented exhibit various effective Nusselt number scalings $Nu \propto Ra^b$. The exponent changes from $b \approx 1/3$ to $b \approx 1/2$ when the Ra number increases beyond the critical value $Ra_* \simeq 6 \times 10^{14}$ ($Pr = 0.7$) and $Ra_* \simeq 6 \times 10^{11}$ ($Pr = 0.021$), respectively. This is consistent with the literature. Furthermore, our results suggest that the transition to the ultimate regime is correlated with a relative enhancement of the temperature-velocity cross-correlations in the bulk of the fluid as hypothesised by Kraichnan, R. H., *Phys. Fluids*, **5**, 1374 (1962).

Key words: Authors should not enter keywords on the manuscript, as these must be chosen by the author during the online submission process and will then be added during the typesetting process (see <http://journals.cambridge.org/data/relatedlink/jfm-keywords.pdf> for the full list)

1. Introduction

Rayleigh–Bénard (RB) convection is a canonical problem for buoyancy-driven flows that are encountered in various technological and geophysical applications (for an overview see Chillà & Schumacher 2012). Typical set-ups are either cylindrical or rectangular as sketched in figure 1. Fluid is confined between the heated wall (T_{hw}) at the bottom and the cooled wall (T_{cw}) at the top held at the temperature difference $\Delta T = T_{hw} - T_{cw}$. The vertical and lateral length scales are L and D ($D = 2R$ for a cylinder with radius R), respectively. For large aspect ratios, $\Gamma = D/L \rightarrow \infty$, the flow is governed by the Rayleigh number Ra and the Prandtl number Pr ,

$$Ra = \frac{g\beta \Delta T L^3}{\nu\kappa}, \quad Pr = \frac{\nu}{\kappa}, \quad (1.1a, b)$$

† Email address for correspondence: marten.klein@b-tu.de

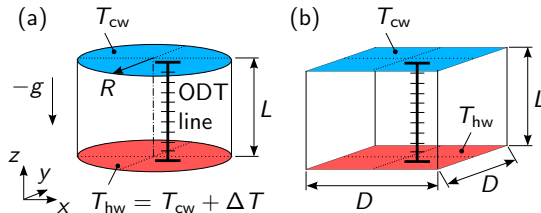


FIGURE 1. Schematic of a (a) cylindrical and (b) rectangular Rayleigh-Bénard set-up. The computational domain for the stochastic one-dimensional turbulence (ODT) simulations is, for both cases, a statistically representative wall-normal vertical line (ODT line).

where g is the constant background gravity, and ν , κ and β are the constant kinematic viscosity, thermal diffusion and thermal expansion coefficients of the fluid, respectively. Both Ra and Pr encompass several orders of magnitude in applications. Ra reaches easily up to 10^{27} and Pr takes values in between 10^{-7} – 10^{23} (Chillà & Schumacher 2012). Here we consider $Pr = 0.7$ (air) and $Pr = 0.021$ (mercury) for a wide range of Ra numbers.

Transitions occur when the Ra number is varied (Malkus 1954; Grossmann & Lohse 2000, among others) and these manifest themselves in the Nusselt number,

$$Nu = \frac{Q}{Q_c} = 1 + \frac{\langle w'T' \rangle_{V,t}}{\kappa \Delta T/L}, \quad (1.2)$$

which is the ratio of the total, Q , and the purely conductive heat transfer, Q_c . The rightmost expression in equation (1.2) relates Nu to the mean turbulent temperature flux per unit area, $\langle w'T' \rangle_{V,t}$, for the present configuration, where $\langle \cdot \rangle$ denotes a Reynolds average under statistically stationary conditions and $(\cdot)'$ the corresponding fluctuations; the subscripts V and t indicate domain-volume and temporal averaging, respectively,

A transition to the ultimate regime of convection is expected for very high Ra numbers when the boundary layer becomes fully turbulent (Kraichnan 1962; Grossmann & Lohse 2000). For fixed Pr , the classical $Nu \propto Ra^{1/3}$ scaling (Malkus 1954) is in turn replaced by $Nu \propto Ra^{1/2} [\ln(Ra)]^{-3/2}$ (Kraichnan 1962). For $Pr \simeq 1$, there is evidence from laboratory experiments that the transition occurs for the critical Rayleigh number $Ra_* \simeq 10^{14}$ (He *et al.* 2012; Chillà & Schumacher 2012, and references therein). This is supported by recent two-dimensional direct numerical simulations (2-D DNSs) that have reached $Ra = 10^{14}$ (Zhu *et al.* 2018). 3-D DNSs, however, have remained in the classical regime by having reached $Ra = 2 \times 10^{12}$ (Stevens *et al.* 2011). For $Pr \ll 1$, the transition to the ultimate regime is expected for lower Ra numbers (Grossmann & Lohse 2000). The critical Rayleigh number is $Ra_* \simeq 10^{11}$ for $Pr \simeq 0.02$ (Chavanne *et al.* 1997; Schumacher *et al.* 2016; Ahlers *et al.* 2017). 3-D DNSs have reached $Ra = 4 \times 10^8$, which is still in the classical regime (Schumacher *et al.* 2016). Unfortunately, there is no 2-D DNS data available that would support or disprove the expected transition and even the available laboratory measurements are not conclusive (e.g. Niemela *et al.* 2000). Complications arise because a $Nu \propto Ra^{1/2}$ scaling, or its onset, may as well be due to roughness (Zhu *et al.* 2019) or non-Oberbeck–Boussinesq effects (Urban *et al.* 2019).

Therefore, the main aim of this paper is to contribute to the controversy by presenting numerical evidence for the transition to the ultimate regime of Rayleigh–Bénard turbulence by utilising the stochastic one-dimensional turbulence (ODT) model (Kerstein 1999; Wunsch & Kerstein 2005). This lower-order modelling approach exhibits a direct turbulence cascade (Kerstein 1999) and might be, in this sense, more representative for 3-D (Kolmogorov) turbulence than 2-D DNSs. Here we specifically limit our attention to a Boussinesq fluid confined between two smooth isothermal no-slip walls.

The rest of this paper is structured as follows. In section 2 we give an overview of the model formulation. In section 3 we present ODT simulation results in terms of bulk profiles, Nusselt numbers, conventional temperature statistics, and temperature-velocity cross-correlations. In section 4 we summarise and conclude our findings.

2. Model formulation

The ODT computational domain is a representative vertical line as shown in figure 1. The flow variables are resolved on all relevant scales along this line and evolved in time by deterministic and stochastic processes (Kerstein 1999). For this study, we have extended the model formulation of Wunsch & Kerstein (2005) to three velocity components analogously to Kerstein *et al.* (2001) within the dynamically-adaptive framework of Lignell *et al.* (2013). In the following, we give a brief but complete overview of the model formulation but defer the reader to the literature for additional technical details.

2.1. Governing equations

The governing equations are the conservation equations of mass, momentum, and energy plus an equation of state. Here we make use of the Oberbeck–Boussinesq approximation with a linear equation of state, $\rho(T) = \rho_0 [1 - \beta(T - T_0)]$, where ρ is the weakly fluctuating density in addition to the other variables; the subscript 0 denotes background values. The density is taken as a constant except for the buoyancy forces, which yields the governing equations as (Kerstein *et al.* 2001; Wunsch & Kerstein 2005)

$$\frac{\partial u_i}{\partial t} + \mathcal{E}_i(\alpha) = \nu \frac{\partial^2 u_i}{\partial z^2}, \quad \frac{\partial T}{\partial t} + \mathcal{E}_T = \kappa \frac{\partial^2 T}{\partial z^2}, \quad (2.1a, b)$$

where $(u_i) = (u, v, w)^T$ denotes the Cartesian velocity components, t the time and z the vertical coordinate. Both $\mathcal{E}_i(\alpha)$ and \mathcal{E}_T are stochastic terms modelling the effects of turbulent advection (Kerstein 1999). In addition, $\mathcal{E}_i(\alpha)$ includes the effects of buoyancy (Wunsch & Kerstein 2005) and fluctuating pressure-gradient forces (Kerstein *et al.* 2001), which are controlled by the model parameter $0 \leq \alpha \leq 1$ (see below). Molecular diffusion is, by contrast, taken as a continuous deterministic process that is treated numerically with a finite-volume method and an explicit time-stepping scheme (Lignell *et al.* 2013).

2.2. Stochastic eddy events

$\mathcal{E}_i(\alpha)$ and \mathcal{E}_T are formulated with the aid of discrete mapping (eddy) events. Conservation and scale-locality properties are addressed by the measure-preserving triplet map (Kerstein 1999). This map compresses flow profiles over a given line interval $z_0 \leq z \leq z_0 + l$ (size l) to one third, pastes two copies to fill the interval, and flips the central copy to ensure continuity. Fluid is instantaneously moved from location $f(z)$ to the mapped location z , which yields

$$\mathcal{E}_i(\alpha) : u_i(z, t) \rightarrow u_i(f(z), t) + c_i(\alpha)K(z), \quad \mathcal{E}_T : T(z, t) \rightarrow T(f(z), t), \quad (2.2a, b)$$

where $K(z) = z - f(z)$ is a kernel function related to the fluid displacement and $c_i(\alpha)$ are coefficients that account for momentum sources and sinks due to fluctuating pressure and buoyancy forces. From Kerstein *et al.* (2001) and Wunsch & Kerstein (2005) we obtain

$$c_i(\alpha) = \frac{1}{K_K} \left[-u_{i,K} + \operatorname{sgn}(u_{i,K}) \sqrt{(1 - \alpha)\tilde{u}_{i,K}^2 + \frac{\alpha}{2}\tilde{u}_{j,K}^2 + \frac{\alpha}{2}\tilde{u}_{k,K}^2} \right], \quad (2.3)$$

where (ijk) are permutations of (123) and $\tilde{u}_{i,K}^2 \equiv u_{i,K}^2 + 2K_K \gamma_i g\beta T_K$, in which $\gamma_i \geq 0$ with $\sum_{i=1}^3 \gamma_i = 1$ are newly introduced weights that control the conversion between the potential and the kinetic energy per component u_i . The kernel-weighted terms follow from the literature: $K_K = \int K^2(z) dz$ and $\phi_K = \int \phi(f(z), t) K(z) dz$ for $\phi = u_i, T$.

For $T_K > 0$, potential energy is released to the vertical velocity component by selecting $(\gamma_i) = (0, 0, 1)^T$. When at the same time $\alpha > 0$, however, some potential energy is directly transferred to the other velocity components due to implied pressure-velocity couplings. For $T_K \leq 0$, kinetic energy is extracted from all three components u_i . This is constrained by c_i being real-valued and addressed by selecting γ_i as the fraction of the available kinetic energy that resides in the component u_i , that is, $\gamma_i = u_{i,K}^2 / \sum_{j=1}^3 u_{j,K}^2$.

Note that the original velocity vector formulation of Kerstein *et al.* (2001) is recovered for $g = 0$ or $\beta = 0$. Likewise, the buoyancy formulation of Wunsch & Kerstein (2005) is recovered for $\alpha = 0$ and $(\gamma_i) = (1, 0, 0)^T$ together with a single-velocity initial condition $u_0 \neq 0, v_0 = w_0 = 0$. The remaining but tiny difference is the numerical evaluation of K_K , which, for fine grids, converges to $(4/27)l^3$ as in the references above.

A stochastic sequence of ODT eddy events aims to mimic the statistical properties of a featureless turbulent flow that, for thermal convection, is conceptually close to the assumptions made by Kraichnan (1962). Each eddy event is described by the random variables location z_0 and size l for a given time t . These variables have to be sampled from the eddy-rate distribution $\lambda(l, z_0; t) = l^{-2} \tau^{-1}(l, z_0; t)$, which is general unknown.

A thinning-and-rejection method is used in practice to avoid the construction of λ (Kerstein 1999). The eddy rate τ^{-1} is in turn estimated locally from the flow state, for example, by adopting a local interpretation of Prandtl's mixing length (Kerstein 1999). Here we use an energetic formulation (Kerstein *et al.* 2001; Wunsch & Kerstein 2005),

$$\tau^{-1} \simeq C \sqrt{\frac{1}{l^6} (u_K^2 + v_K^2 + w_K^2) + \frac{2K_K}{l^6} g\beta T_K - Z \frac{\nu^2}{l^4}}, \quad (2.4)$$

where C is the ODT eddy-rate parameter and the individual terms under the square root represent the available kinetic, potential, and a viscous penalty energy. The latter effectively suppresses eddy events below the Kolmogorov length scale (Kerstein 1999). Therefore, Z is the ODT small-scale (viscous) suppression parameter. Candidate eddy events are deemed unphysical and rejected when τ^{-1} is imaginary. Otherwise they are accepted with probability $\tau^{-1}/\tau_s^{-1} \ll 1$, where τ_s^{-1} is the mean sampling rate of a marked Poisson process (Kerstein 1999). Note that no large-scale suppression method is used here so that eddy events up to the full height, $l = L$, are possible but rare.

2.3. Model validation for turbulent Rayleigh–Bénard convection

Building on the extensive model validation by Wunsch & Kerstein (2005), we estimated the model parameters C and Z for fixed $\alpha = 2/3$ and γ_i from above. We used reference data from Stevens *et al.* (2011), Li *et al.* (2012), and Schumacher *et al.* (2016) for only two pairs (Pr, Ra) as indicated in figure 3. This yielded $C = 60$ for $Pr = 0.7$, $C = 43$ for $Pr = 0.021$, and $Z = 220$ for both Pr (Klein & Schmidt 2019; Klein *et al.* 2018).

3. Results

In the following, the model parameters are kept fixed in order to emphasise the predictive capabilities of the ODT modelling approach. We vary Ra for $Pr = 0.7$ and $Pr = 0.021$, respectively, in order to address the transition to the ultimate regime.

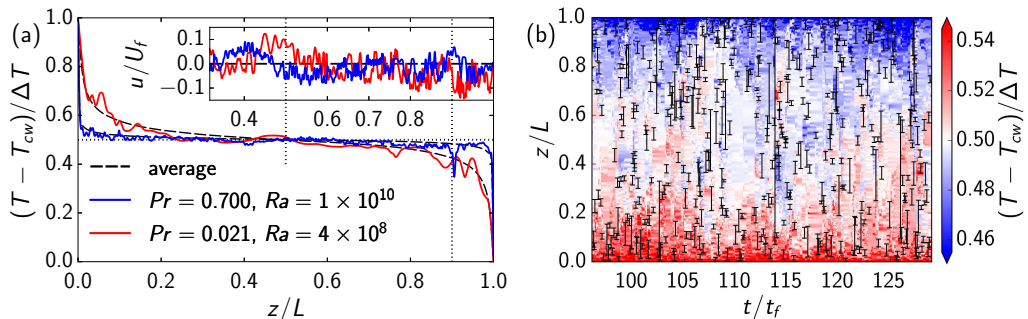


FIGURE 2. (a) Vertical profiles of the instantaneous, T , and time-averaged temperature, $\langle T \rangle$, together with the instantaneous wall-tangential velocity u (inset). Two cases with different Pr but similar $Gr = Ra/Pr = (1.6 \pm 0.3) \times 10^{10}$ are shown. Dotted lines are given for orientation. (b) Space-time diagram of the ODT instantaneous temperature for $Pr = 0.7, Ra = 10^{10}$. Black vertical lines explicitly mark every 10th instantaneous eddy event. $U_f = \sqrt{g\beta\Delta T L}$ is the free-fall velocity and $t_f = L/U_f$ the free-fall time.

3.1. Bulk profiles

Figure 2(a) shows profiles of the instantaneous, T , and the time-averaged temperature, $\langle T \rangle$, together with profiles of the instantaneous wall-tangential velocity component u for the two Prandtl numbers investigated. The cases shown exhibit approximately the same Grashof number $Gr = Ra/Pr = (1.6 \pm 0.3) \times 10^{10}$. The spatial scales in the instantaneous velocity fields are therefore comparable for both cases. They are also comparable to the spatial scales in the temperature field for $Pr = 0.7$ since the thermal and viscous diffusion time scales are similar. By contrast, the spatial scales seen in the temperature field are larger for the lower $Pr = 0.021$ due to faster thermal diffusion. Furthermore, the mean temperature profiles are smooth and symmetric to the mid-height, $z/L = 0.5$, which indicates well-behaved grid adaption with negligible numerical transport. Note that the mean velocity is zero here because the mean and large-scale flow (see, for example, Shraiman & Siggia 1990) is not resolved by ODT.

Figure 2(b) shows a space-time diagram of an ODT temperature solution. One can see that eddy events may displace fluid over large distances. This can be viewed as trace of plumes in the ODT model. The small-scale eddy events tend to follow a direct cascade, which is here likely caused by large velocity gradients on the small scales (see figure 2(a)).

3.2. Nusselt number

The Ra dependence of the Nu number is investigated for $Pr = 0.7$ and 0.021 by stochastic ODT simulations. The ODT model parameters are kept constant to address the predictive capabilities of the model. Nu is computed according to equation (1.2) for the 1-D computational domain by long-time averaging over several hundred thousand (low Ra) to several million (high Ra) eddy events in the statistically stationary state. Confidence margins are obtained by computing Nu in the upper and lower half of the domain and these show sufficiently converged results. The Rayleigh numbers investigated encompass $10^8 \leq Ra \leq 10^{16}$ for $Pr = 0.7$ and $10^5 \leq Ra \leq 8 \times 10^{13}$ for $Pr = 0.021$. This is an extension of the high- Ra preliminary results in Klein & Schmidt (2019).

Figure 3 shows $Nu(Ra)$ for $Pr = 0.7$ and 0.021 , respectively. ODT simulation results are given together with available reference data from DNS and laboratory measurements, which encompass a range of aspect ratios and Pr numbers. For very large Ra numbers, the log-corrected theoretical scaling $Nu \propto Ra^{1/2} [\ln(Ra)]^{-3/2}$ (Kraichnan 1962) serves as a reference. The Nu numbers shown in figure 3(a) indicate very good agreement between

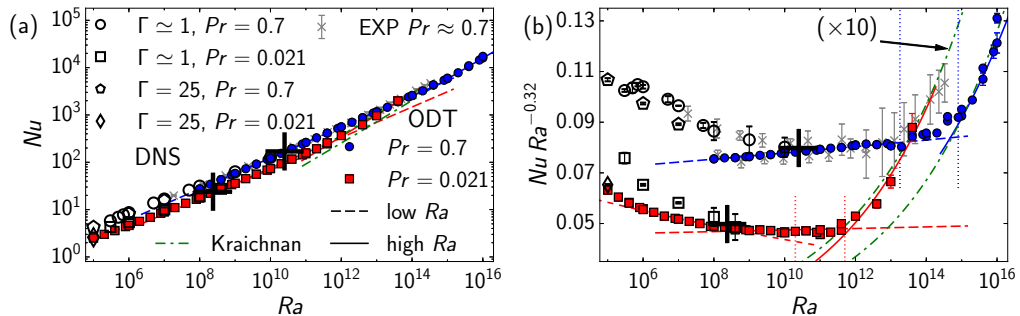


FIGURE 3. (a) Nusselt number Nu over Rayleigh number Ra for the Prandtl numbers $Pr = 0.7$ and 0.021 , respectively. (b) Same data but compensated with $Ra^{0.32}$. ODT results and the corresponding scaling laws are given. ODT validation cases for the Pr -dependent prefactor are marked by ‘+’ (Klein & Schmidt 2019). Reference DNS data are given for $1 \leq \Gamma \leq 3$, $Pr = 0.7$ (Scheel & Schumacher 2014); $\Gamma = 1$, $Pr = 0.021$ (Scheel & Schumacher 2016; Schumacher *et al.* 2016); $\Gamma = 25$, $Pr = 0.7$ and 0.021 (Pandey *et al.* 2018). Reference measurement data (EXP) encompass $0.23 \leq \Gamma \leq 20$, $0.5 \leq Pr \leq 10$ (Chillà & Schumacher 2012, and references therein). Transitional Ra ranges are marked by dotted lines (He *et al.* 2012; Schumacher *et al.* 2016). The Kraichnan (1962) scaling received an empirically magnified prefactor ($\times 10$) for $Pr = 0.021$.

Pr	Ra_{min}	Ra_{max}	a	b	a_{ref}	b_{ref}
0.7	10^8	10^{13}	0.066 ± 0.001	0.32 ± 0.01	$0.15 \pm 0.01^\dagger$	$0.29 \pm 0.01^\dagger$
0.7	10^{15}	10^{16}	$(1.1 \pm 0.3) \times 10^{-3}$	0.44 ± 0.02	$0.78 \times 10^{-3}\ddagger$	0.458^\ddagger
0.021	10^6	5×10^8	0.078 ± 0.001	0.29 ± 0.01	$0.15 \pm 0.04^\dagger$	$0.26 \pm 0.01^\dagger$
0.021	10^9	5×10^{11}	0.044 ± 0.005	0.32 ± 0.01	$0.45 \pm 0.10^*$	$0.28 \pm 0.01^*$
0.021	10^{12}	8×10^{13}	$(1.5 \pm 0.3) \times 10^{-3}$	0.45 ± 0.02	$1.50 \times 10^{-3}\ddagger (\times 10)$	0.449^\ddagger

TABLE 1. ODT scaling laws $Nu = a Ra^b$ across $Ra_{min} \leq Ra \leq Ra_{max}$ for various Pr . Reference values a_{ref} , b_{ref} are from Scheel & Schumacher (2014, 2016, \dagger), Shraiman & Siggia (1990, $*$), and Kraichnan (1962, \ddagger). The prefactors of the Kraichnan theory are $\tilde{a} \approx 0.037$ ($Pr = 0.7$) and $\tilde{a} \approx 0.0054$ ($Pr = 0.021$), where latter demands an empirical magnification ($\times 10$) to fit the data.

the present ODT results and the available reference data across eight decades of the Ra number for each Prandtl number. All the ODT simulation runs together consumed ≈ 24000 CPU-h on local workstations equipped with Intel[®] Xeon[®] 2.40 GHz CPUs.

Figure 3(b) shows Nu compensated with $Ra^{0.32}$ to aid the quantitative analysis. The ODT data for fixed Pr exhibit various effective scaling laws $Nu = a Ra^b$. These have been obtained by a least-squares fit and are summarised in table 1. For $Ra < 10^{13}$ ($Pr = 0.7$) and $Ra < 5 \times 10^{11}$ ($Pr = 0.021$), ODT exhibits the classical scaling close to $Nu \propto Ra^{1/3}$ in agreement with Malkus (1954). A relative decrease of the exponent to $Nu \propto Ra^{2/7}$ (Shraiman & Siggia 1990) is only observed for $Pr = 0.021$, $Ra < 10^9$ but not for $Pr = 0.7$. Interestingly, for $Pr = 0.021$, $Ra = 10^5$, ODT reproduces the reference value of Pandey *et al.* (2018), which has been obtained for a large-aspect-ratio RB cell ($\Gamma = 25$). This suggests that the ODT formulation is consistent with $\Gamma \gg 1$ and is, thus, complementary to DNS and laboratory experiments with $\Gamma \lesssim 1$. We conjecture that small-aspect-ratio effects (like the unresolved large-scale circulation) together with the energetically bounded Ra range ($Ra \geq 10^5 Z Pr$; see Wunsch & Kerstein 2005) are the main reasons for the different scaling of the ODT results observed for $Ra < 10^9$.

Moving on to high Ra numbers, the transition to the ultimate regime is expected for $1.8 \times 10^{13} \leq Ra \leq 8 \times 10^{14}$ ($Pr = 0.7$; He *et al.* 2012; Chillà & Schumacher 2012, and

references therein) and $2 \times 10^{10} \leq Ra \leq 5 \times 10^{11}$ ($Pr = 0.021$; Schumacher *et al.* 2016; Ahlers *et al.* 2017). It is remarkable that the ODT results exhibit a transition within the expected Ra ranges for fixed model parameters. The critical Ra_* numbers obtained with ODT are at the upper limits of these ranges, that is, $Ra_* \simeq 6 \times 10^{14}$ for $Pr = 0.7$ and $Ra_* \simeq 6 \times 10^{11}$ for $Pr = 0.021$, respectively. The aspect ratio might influence Ra_* indirectly by favouring some mean and large-scale motions that feed back on the boundary layer transition. In ODT, the such motions are absent by construction.

It is remarkable also that the present ODT results are in very good agreement with the Kraichnan (1962) theory by closely following $Nu \simeq \tilde{a}(Pr) Ra^{1/2} [\ln(Ra)]^{-3/2}$ for the highest Ra numbers investigated. For $Pr = 0.7$, Kraichnan's prefactor $\tilde{a} \simeq 0.0089 Pr^{-4} \approx 0.037$ yields an almost perfect match between the asymptotic theory and ODT. For $Pr = 0.021$, however, $\tilde{a} \simeq 0.037 Pr^{1/2} \approx 0.0054$ is by a factor ≈ 10 too small. The reason for the disagreement is unclear but might be related to the fact that much higher Ra numbers are targeted by the Kraichnan (1962) theory. We emphasise here that the present ODT results are otherwise consistent with the available reference data (see below).

3.3. Conventional temperature statistics

Vertical profiles of temperature statistics have been obtained for a diagnostic grid by interpolating and time-averaging instantaneous profiles. We consider the non-dimensional mean temperature Θ and standard deviation of the temperature fluctuations σ ,

$$\Theta(z) = (\langle T \rangle(z) - T_b) / \Delta T, \quad \sigma(z) = \sqrt{\langle T^2 \rangle(z) - \langle T \rangle^2(z)} / \Delta T, \quad (3.1a, b)$$

where $\langle \cdot \rangle$ denotes time-averaging and $T_b = (T_{hw} + T_{cw}) / 2$ is the bulk temperature for the present configuration (compare with figure 2).

Figure 4 shows Θ and σ according to equations (3.1a, b) for $Pr = 0.7$ and 0.021, respectively. Here σ is normalised by its maximum value σ_{max} in order to focus on the shapes. Available reference DNS data are shown for comparison. The flow statistics are symmetric to the mid-height so that we present data only for the lower half of the domain ($z/L \leq 0.5$). At the wall, the heat transport is entirely carried by molecular diffusion so that Nu is related to the wall-temperature gradient, $Nu = -(\mathrm{d}\langle T \rangle / \mathrm{d}z)_{hw} / (\Delta T / L)$. This yields the thermal boundary layer thickness as $\delta / L = (2Nu)^{-1}$, which is given in figure 4 and indicates that the resolution is high enough to resolve all relevant features.

In general, Θ and σ are well-captured by ODT in the vicinity of the wall and further towards the bulk for both Pr numbers investigated. For $Pr = 0.7$ in figures 4(a, b), one can discern a spurious, undulating structure in the ODT results for finite distances from the wall, $2 \times 10^{-3} \lesssim z/L \lesssim 10^{-2}$. This feature is a modelling artefact, which is related to the triplet map (Lignell *et al.* 2013). Interestingly, this feature has disappeared for $Pr = 0.021$ in figures 4(c, d). We attribute this effect to the larger thermal diffusivity in the case of a lower Pr number. The turbulence is also more vigorous and, considering the velocity field, exhibits a broader range of scales. So, not only molecular but also turbulent processes contribute to diffuse the imprint of the near-wall self-similar mapping. This is, in fact, consistent with the effects observed for a smaller ODT viscous suppression parameter Z (see Klein *et al.* 2018).

The ODT simulated profiles $\Theta(z)$ and $\sigma(z)$ exhibit a logarithmic region in the classical and ultimate regime when the Ra number is large enough. The profiles take the form

$$\Theta(z) = A \ln(z/L) + B, \quad \sigma(z) = C \ln(z/L) + D, \quad (3.2a, b)$$

where the coefficients A, B, C, D are obtained by a least-squares fit across $10^{-2} \leq z/L \leq 10^{-1}$. These fits are shown as dotted lines in figure 4, where only $Ra = 10^5$ for $Pr = 0.021$

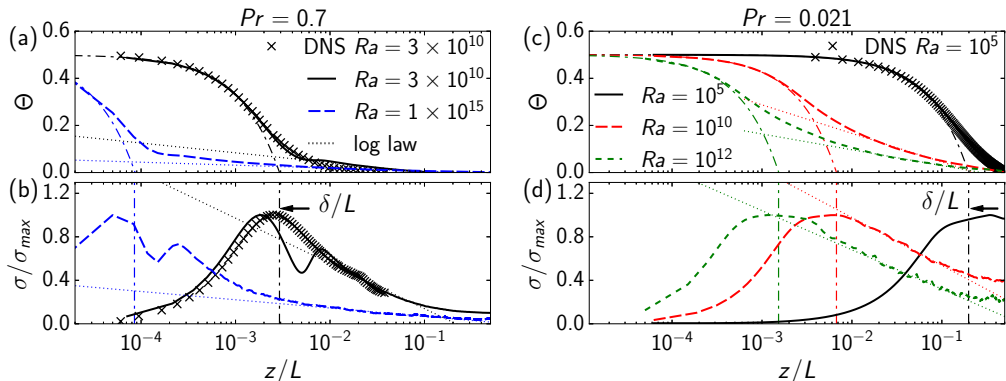


FIGURE 4. Temperature statistics in the lower half of the domain for (a,b) $Pr = 0.7$ and (c,d) $Pr = 0.021$. (a,c) Non-dimensional mean temperature Θ . Dash-dotted lines give the linearly extrapolated wall gradient. (b,d) Standard deviation σ of the temperature fluctuations. Dotted lines show equations (3.2a, b) fitted to the ODT data across $10^{-2} \leq z/L \leq 10^{-1}$. Vertical dash-dotted lines mark the thermal boundary layer thickness $\delta/L = (2Nu)^{-1}$. Reference DNS data for $Pr = 0.7$ are from Li *et al.* (2012) for the centre-line of a cylindrical set-up with $\Gamma = 1$, whereas for $Pr = 0.021$ they are from Pandey *et al.* (2018) for a rectangular set-up with $\Gamma = 25$.

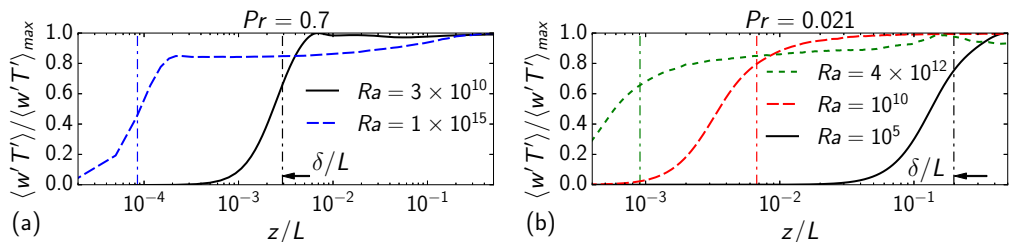


FIGURE 5. Temperature-velocity cross-correlations $\langle w'T' \rangle$ in the lower half of the domain for (a) $Pr = 0.7$ and (b) $Pr = 0.021$. Vertical lines mark the thermal boundary layer thickness δ as in figure 4.

has been excluded as it does not exhibit a logarithmic region. The coefficients A and C approach zero from below with increasing Ra number. All of these aspects are in very good qualitative agreement with Ahlers *et al.* (2012).

3.4. Temperature-velocity cross-correlations

The temperature-velocity cross-correlations $\langle w'T' \rangle$ are computed in ODT on the basis of the map-induced changes (Kerstein 1999). Cross-correlations are therefore rather well captured even when the auto-correlation of the fluctuations themselves is underestimated (Kerstein 1999; Kerstein *et al.* 2001; Klein *et al.* 2019). We make use of this property of the model to gain further insight into the boundary layer for different convection regimes.

Figure 5 shows vertical profiles of the temperature-velocity cross-correlations $\langle w'T' \rangle$ obtained with ODT for the lower half of the domain. The data have been normalised with the maximum value $\langle w'T' \rangle_{max}$ in order to focus on the shapes. In the classical regime, for $Pr = 0.7$, $Ra = 3 \times 10^{10}$ in figure 5(a), $\langle w'T' \rangle$ increases rapidly across the conductive sub-layer so that the maximum value is reached at $z/L \approx 2\delta/L \approx 6 \times 10^{-3}$. This is similar for $Pr = 0.021$, $Ra = 10^{10}$ in figure 5(b). By contrast, the case $Pr = 0.021$, $Ra = 10^5$ in figure 5(b), is dominated by thermal diffusion since the conductive sub-layer extends up to $z/L = 2\delta/L \approx 0.4$ and $\langle w'T' \rangle$ peaks at mid-height.

In the ultimate regime, for $Pr = 0.7$, $Ra = 10^{15}$ in figure 5(a), $\langle w'T' \rangle$ has only reached

$\approx 82\%$ of its maximum value at $z/L = 2\delta/L \approx 2 \times 10^{-4}$. The temperature-velocity cross-correlation increases further with distance, but more gradually, and attains its maximum value in the bulk for $z/L \gtrsim 0.18$. A similar behaviour can be discerned for $Pr = 0.021$, $Ra = 4 \times 10^{12}$ in figure 5(b), where $\langle w'T' \rangle$ reaches only $\approx 75\%$ of its maximum value at $z/L = 2\delta/L \approx 2 \times 10^{-3}$. Likewise, the maximum temperature-velocity cross-correlation obtained with ODT is reached around $z/L \approx 0.18$, but reduces again towards the mid-height. This effect is robustly observed also for the higher Ra numbers investigated.

We note that the shape differences exhibited by $\langle w'T' \rangle$ for $Pr = 0.7$, $Ra = 3 \times 10^{10}$ and $Pr = 0.021$, $Ra = 10^{10}$ across the interval $10^{-3} \leq z/L \leq 10^{-2}$ are related to the map-based advection representation analogously to the discussion of figure 4 above.

4. Conclusion

One-dimensional turbulence (ODT) simulations of high- Ra thermal convection were conducted for $Pr = 0.7$ and 0.021 , respectively, in order to numerically address the transition to the ultimate regime. ODT is a stochastic turbulence model that aims to resolve all relevant scales of the turbulent flow for a wall-normal vertical line. This model effectively mimics the direct cascade of featureless Kolmogorov turbulence within the dimensionally-reduced setting. Here we have considered a Boussinesq fluid confined between smooth isothermal no-slip walls for a configuration with infinite aspect ratio.

For fixed Pr and ODT parameters, the ODT model captures the classical $Nu \propto Ra^{1/3}$ scaling and the onset of the ultimate regime by realising $Nu \simeq \tilde{a}(Pr) Ra^{1/2} [\ln(Ra)]^{-3/2}$. In the classical regime, ODT only slightly overestimates the scaling exponent of the available reference data. The transition to the ultimate regime is observed for the critical Rayleigh numbers $Ra_* \simeq 6 \times 10^{14}$ ($Pr = 0.7$) and $Ra_* \simeq 6 \times 10^{11}$ ($Pr = 0.021$), respectively. These values are within the ranges given in the literature but close to the upper limits (He *et al.* 2012; Schumacher *et al.* 2016; Ahlers *et al.* 2017). In the ultimate regime, ODT results are remarkably well described by the Kraichnan (1962) theory. This includes the prefactor \tilde{a} for $Pr = 0.7$, but not for $Pr = 0.021$ for which it is an order of magnitude too small. The reason for this discrepancy is unclear since otherwise the ODT results are consistent with the available reference data. The slightly different classical scaling and the late transition are presumably related to unresolved large-scale motions.

At last, we note that the ODT results exhibit logarithmic temperature profiles prior and after the transition to the ultimate regime for large Ra numbers. This is in agreement with the literature (Ahlers *et al.* 2012). After the transition, however, ODT yields a relative enhancement of the temperature-velocity cross-correlations in the bulk of the fluid. This gives numerical support to an analogous assumption of Kraichnan (1962).

Acknowledgements

We thank Amrish Pandey for providing DNS reference data. Financial support by the European Regional Development Fund (EFRE), Grant No. StaF 23035000, and the German Academic Exchange Service (DAAD), which is funded by the Federal Ministry of Education and Research (BMBF), Grant No. ID-57316240, is kindly acknowledged.

REFERENCES

- AHLERS, G., BODENSCHATZ, E., FUNFSCHILLING, D., GROSSMANN, S., HE, X., LOHSE, D., STEVENS, R. J. A. M. & VERZICCO, R. 2012 Logarithmic temperature profiles in turbulent Rayleigh–Bénard convection. *Phys. Rev. Lett.* **109**, 114501.

- AHLERS, G., BODENSCHATZ, E. & HE, X. 2017 Ultimate-state transition of turbulent Rayleigh–Bénard convection. *Phys. Rev. Fluids* **2**, 054603.
- CHAVANNE, X., CHILLÀ, F., CASTAING, B., HÉBRAL, B., CHABAUD, B. & CHAUSSY, J. 1997 Observation of the ultimate regime in Rayleigh–Bénard convection. *Phys. Rev. Lett.* **79** (19), 3648–3651.
- CHILLÀ, F. & SCHUMACHER, J. 2012 New perspectives in turbulent Rayleigh–Bénard convection. *Eur. Phys. J. E* **35**, 58.
- GROSSMANN, S. & LOHSE, D. 2000 Scaling in thermal convection: A unifying theory. *J. Fluid Mech.* **407**, 27–56.
- HE, X., FUNFSCHILLING, D., NOBACH, H., BODENSCHATZ, E. & AHLERS, G. 2012 Transition to the ultimate state of turbulent Rayleigh–Bénard convection. *Phys. Rev. Lett.* **108**, 024502.
- KERSTEIN, A. R. 1999 One-dimensional turbulence: Model formulation and application to homogeneous turbulence, shear flows, and buoyant stratified flows. *J. Fluid Mech.* **392**, 277–334.
- KERSTEIN, A. R., ASHURST, W. T., WUNSCH, S. & NILSEN, V. 2001 One-dimensional turbulence: Vector formulation and application to free shear flows. *J. Fluid Mech.* **447**, 85–109.
- KLEIN, M. & SCHMIDT, H. 2019 Investigating Rayleigh–Bénard convection at low Prandtl numbers using one-dimensional turbulence modeling. In *Proc. 11th Int. Symp. Turb. Shear Flow Phen. (TSFP11)*. Southampton, UK, in press (to appear August 2019).
- KLEIN, M., SCHMIDT, H. & LIGNELL, D. O. 2018 Map-based modeling of high-Rayleigh-number turbulent convection in planar and spherical confinements. In *Proc. Conf. Model. Fluid Flow (CMFF'18)* (ed. J. Vad). Budapest, Hungary, ISBN 978-963313297-5.
- KLEIN, M., ZENKER, C. & SCHMIDT, H. 2019 Small-scale resolving simulations of the turbulent mixing in confined planar jets using one-dimensional turbulence. *Chem. Eng. Sci.* **204**, 186–202.
- KRAICHNAN, R. H. 1962 Turbulent thermal convection at arbitrary Prandtl number. *Phys. Fluids* **5**, 1374.
- LI, L., SHI, N., DU PUIITS, R., RESAGK, C., SCHUMACHER, J. & THESS, A. 2012 Boundary layer analysis in turbulent Rayleigh–Bénard convection in air: Experiment versus simulation. *Phys. Rev. E* **86**, 026315.
- LIGNELL, D. O., KERSTEIN, A. R., SUN, G. & MONSON, E. I. 2013 Mesh adaption for efficient multiscale implementation of one-dimensional turbulence. *Theor. Comp. Fluid Dyn.* **27** (3), 273–295.
- MALKUS, W. V. R. 1954 Discrete transitions in turbulent convection. *Proc. Royal Soc. A* **225**, 185–195.
- NIEMELA, J. J., SKRBEK, L., SREENIVASAN, K. R. & DONNELLY, R. J. 2000 Turbulent convection at very high Rayleigh numbers. *Nature* **404**, 837–840.
- PANDEY, A., SCHEEL, J. D. & SCHUMACHER, J. 2018 Turbulent superstructures in Rayleigh–Bénard convection. *Nature Comm.* **9**, 2118.
- SCHEEL, J. D. & SCHUMACHER, J. 2014 Local boundary layer scales in turbulent Rayleigh–Bénard convection. *J. Fluid Mech.* **758**, 344–373.
- SCHEEL, J. D. & SCHUMACHER, J. 2016 Global and local statistics in turbulent convection at low Prandtl numbers. *J. Fluid Mech.* **802**, 147–173.
- SCHUMACHER, J., BANDARU, V., PANDEY, A. & SCHEEL, J. D. 2016 Transitional boundary layers in low-Prandtl-number convection. *Phys. Rev. Fluids* **1**, 084402.
- SHRAIMAN, B. I. & SIGGIA, E. D. 1990 Heat transport in high-Rayleigh-number convection. *Phys. Rev. A* **42** (6), 3650–3653.
- STEVENS, R. J. A. M., LOHSE, D. & VERZICCO, R. 2011 Prandtl and Rayleigh number dependence of heat transport in high Rayleigh number thermal convection. *J. Fluid Mech.* **688**, 31–43.
- URBAN, P., HANZELKA, P., KRÁLÍK, T., MACEK, M., MUSILOVÁ, V. & SKRBEK, L. 2019 Elusive transition to the ultimate regime of turbulent Rayleigh–Bénard convection. *Phys. Rev. E* **99**, 011101(R).
- WUNSCH, S. & KERSTEIN, A. R. 2005 A stochastic model for high-Rayleigh-number convection. *J. Fluid Mech.* **528**, 173–205.
- ZHU, X., MATHAI, V., STEVENS, R. J. A. M., VERZICCO, R. & LOHSE, D. 2018 Transition

to the ultimate regime in two-dimensional Rayleigh–Bénard convection. *Phys. Rev. Lett.* **120**, 144502.

ZHU, X., STEVENS, R. J. A. M., SHISHKINA, O., VERZICCO, R. & LOHSE, D. 2019 $Nu \sim Ra^{1/2}$ scaling enabled by multiscale wall roughness in Rayleigh–Bénard turbulence. *J. Fluid Mech.* **869**, R4.